SlpRoF: improving the temporal coverage and robustness of RF-based vital sign monitoring during sleep

Pei Wang, Xujun Ma, Rong Zheng, Luan Chen, Xiaoling Zhang, Djamal Zeghlache, Daqing Zhang

▶ To cite this version:

Pei Wang, Xujun Ma, Rong Zheng, Luan Chen, Xiaoling Zhang, et al.. SlpRoF: improving the temporal coverage and robustness of RF-based vital sign monitoring during sleep. IEEE Transactions on Mobile Computing, 2024, 23 (7), pp.7848 - 7864. 10.1109/TMC.2023.3340925 . hal-04392265

HAL Id: hal-04392265
https://hal.science/hal-04392265v1

Submitted on 27 Nov 2024

SlpRoF: Improving the Temporal Coverage and Robustness of RF-based Vital Sign Monitoring during Sleep

Pei Wang, *Graduate Student Member, IEEE*, Xujun Ma, *Member, IEEE*, Rong Zheng, *Senior Member, IEEE*, Luan Chen, *Member, IEEE*, Xiaolin Zhang, Djamal Zeghlache, *Life Member, IEEE*, and Daqing Zhang, *Fellow, IEEE*

Abstract—Most existing RF-based vital sign monitoring systems either assume that a human subject is stationary or discard measurements when motion is detected in order to output reliable respiration rates and heart rates. Such an assumption greatly limits the usability of these systems in practice. Even during sleep, one can undergo various body states including turns and involuntary twitches in light sleep, motionlessness during deep sleep, or abnormal limb movements due to sleep disorders such as restless legs syndrome. In this work, we develop SlpRoF, a low-cost contact-free system using a commercial-off-the-shelf UWB radar that achieves high temporal coverage and high accuracy in vital sign monitoring during sleep. By classifying body states into the motionless state, limb movement state, and torso movement state, and extracting vital signs during the first two states, it directly increases effective reporting periods over nights. By analyzing high-order harmonics and leveraging spatial diversity in captured signals from multiple on-body areas, it improves the accuracy of heart rate estimations and thus indirectly increases temporal coverage through reliable assessments. Experiment results show that SlpRoF is able to achieve an average median absolute error (MAE) of 0.44 beats per minute (bpm) in respiration rates, 1.55s in respiration intervals, and 0.9 bpm for heart rates, respectively.

Index Terms—Body state classification, heart rates, respiration rates and intervals, sleep physiological profile, UWB radar signal.

◆

1 INTRODUCTION

SLEEP is an essential function of the human body. Both our mental and physical states are recovered from the day's stresses during sleep time. Poor sleep and sleep disorders, on the other hand, are indicative of underlying health problems and can lead to chronic diseases [1]. Respiratory rates, respiratory intervals, and heart rates are the key parameters of one's sleep physiological profile and play important roles in assessing sleep quality and early diagnosis of sleep disorders and apnea [2].

Compared to contact-based sleep monitoring systems such as Polysomnography (PSG), Photoplethysmography (PPG) and wristbands, RF-based sensing approaches are appealing because they neither confine subjects with cables or to beds nor cause discomfort or skin irritation from contacts with electrodes or straps [3]. Liu *et al.* [4] re-use existing WiFi networks for concurrently tracking respiration and heartbeat rates during sleep. Researchers in [5], [6] further develop WiFi-based sleep stage classification systems based on extracted human physiological features during sleep. Leveraging RFID techniques, vital signs [7], sleep activity [8], and sleep postures [9] could be detected. However, narrowband WiFi or RFID signals are susceptible to interfering sources in target environments such as moving fans and other people. Alternatively, impulse radio ultra-wideband (IR-UWB) and frequency-modulated continuous-wave (FMCW) radars have been employed to estimate vital signs or perform prescribed activities of daily living and exercises [10], [11], [12], [13]. Benefiting from their large operating bandwidth, both FMCW and IR-UWB systems can isolate environmental interference and provide detailed sleep physiological measurements. Wang *et al.* [14] propose a robust contact-free vital sign monitoring system with mmWave FMCW radar and camera fusion in the presence of moving people around the subject. In the sleep scenario, Turppa *et al.* [15] leverage cost-effective 24GHz FMCW radar to extract nocturnal respiration signals with different lying positions and abnormal hypopnea. Lee *et al.* [16] utilize an IR-UWB radar to track the vital sign signals and fine movements of neonates and distinguish infants' sleep/wake states in neonatal intensive care units. However, due to complex and volatile sleep states in practical scenarios, existing works suffer from *under-reporting* of vital signs over time, *inability to accurately detect variations* in respiration cycles such as long pauses due to sleep apnea and *inaccuracy in heart rate estimations* in certain body postures. Specifically, they have the following three limitations.

First, existing RF-based vital sign monitoring systems [17], [18], [19], [20] either assume that subjects are station-

---

Pei Wang, Xunjun Ma, Djamal Zeghlache and Daqing Zhang are with the SAMOVAR, Télécom SudParis, Institut Polytechnique de Paris, 91120 Palaiseau, France (e-mail: pei.wang@telecom-sudparis.eu; xujun.ma@telecom-sudparis.eu; djamal.zeghlache@telecom-sudparis.eu; daqing.zhang@telecom-sudparis.eu)

Rong Zheng is with Department of Computing and Software,McMaster University, 1280 Main Street Weest, Hamilton, Ontario, Canada (email: rzheng@mcmaster.ca)

Luan Chen is with the ETIS UMR8051, CY Cergy Paris Université, ENSEA, CNRS, F-95000, Cergy, France (email: luan.chen@ensea.fr)

Xiaolin Zhang is with the Peking University First Hospital, No.1, Xi'anmen Street, Xicheng District, 100034 Beijing, China (email: zhangxiaolin0001@126.com)

Manuscript received 17 May 2023; revised 05 Nov. 2023; accepted XX XXX. XXXX. Date of publication XX XXX. XXXX; date of current version XX XXX.XXXX. (Corresponding author: Xujun Ma.)

ary or discard measurements when motions are detected. Although MoRe-Fi [21] and MoVi-Fi [22] demonstrate the feasibility of motion-robust vital sign monitoring during exercising and sleeping using deep learning models, there has not been much longitudinal study on mmWave based sleep monitoring or testing with real patients suffering from breathing disorders (e.g., apnea and hypopnea) and irregular heart rhythm (e.g., arrhythmia). In practice, over the course of a night, a person can undergo different body motions, including periods of brief movements such as turns and involuntary twitches in light sleep, motionlessness in deep sleep, or abnormal leg movements due to sleep disorders such as restless legs syndrome and periodic limb movement disorder. These body movements result in low reporting rates of vital signs, making these systems clinically unacceptable. Second, existing works estimate respiration intervals by searching peaks of respiratory waveforms with an empirical threshold [23], [24]. However, due to the change of body orientation after frequent body movement, the amplitude of reflected chest waveforms vary dramatically, which will decrease the accuracy of respiration interval estimation. These approaches become unreliable for real sleep scenario, making it unsuitable to detect respiratory anomalies such as apnea and hypopnea in sleep. Third, to estimate heart rate, existing works typically first identify the radar signals that contain the largest respiratory movements, and then extract heart rates from the selected signals by simply finding a peak frequency in a target range, e.g., $1Hz$ to $2Hz$ [25]. However, some harmonics of strong respiration signals have similar or even higher magnitudes compared with the heartbeat signals. Moreover, under certain sleep postures or during strong abdominal breathing, the body areas with the largest respiration and heart beat movements no longer coincide. As a result, existing works fail to estimate heart rates reliably in such situations.

In this paper, we introduce *temporal coverage*, a new performance metric for vital sign monitoring systems, defined as the percentage of time the reported values are within a pre-specified error range. Clearly, temporal coverage is a hybrid measure that accounts for both reporting rates (namely, the percentage of time vital sign estimations are reported) and the accuracy of the estimations. Consequently, we propose SlpRoF, a low-cost, contact-free system that achieves high temporal coverage and high accuracy in vital sign monitoring during sleep. To overcome the first limitation, SlpRoF classifies body movements during sleep into three types: *motionless*, *limb movement*, and *torso movement* states, and estimates the onset and the duration of each state. Noting that it is possible to estimate vital signs reliably during limb movements, we extend reporting periods beyond motionless states, thereby improving the temporal coverage of vital sign monitoring. For handling the second limitation, dynamic thresholds are proposed to identify the end of inhalation in each respiratory cycle, which provides robust estimation of respiration intervals despite signal amplitude variations from body state changes. To address the third limitation, when extracting heartbeat signals, instead of only considering the reflected signals from one specific on-body location with the largest respiration movements, we search for signals containing heartbeat information in the vicinity of such a location. A high-order harmonic-based approach is proposed to separate weak heartbeat signals from strong respiration signals. To avoid outliers, SlpRoF takes the median value of the estimated heart rates from different on-body locations as the final estimation. Doing so indirectly increases temporal coverage through more reliable estimations.

We have implemented SlpRoF using low-cost and commercial-off-the-shelf (COTS) components including an IR-UWB radar and a raspberry Pi device. The hardware platform can be conveniently placed next to one's bed and at the chest height to cover the full human body. Multi-night deployment has been done in a dormitory, a hotel room, and a hospital ward with ten healthy subjects, one patient who suffers from severe apnea, and one infected by COVID-19 [1]. Experiment results demonstrate that SlpRoF can reliably detect different body motion states, and extend the temporal coverage of vital sign reporting. Apart from accurate fine-grained respiratory profiles, SlpRoF also provides reliable heart rate estimations. In summary, there are five main contributions in this work:

- We conduct an extensive measurement study to investigate the impacts of body motion states, sleep postures and abnormal breathing patterns on received radar signal characteristics.
- We propose a method based on the time-frequency domain features of radar signals reflected from different body parts to identify *motionless*, *limb movement*, and *torso movement* states during sleep. The inclusion of vital sign estimation in limb movement state improves the temporal coverage of respiration rate and heart rate reporting by about 16% and 10%, respectively.
- We propose a comprehensive respiratory profiling approach. It applies continuous wavelet transformation (CWT) and two levels of dynamic thresholding to detect the end of inhalation in each breathing cycle. SlpRoF achieves median absolute errors (MAEs) of 0.44 bpm and 1.55s in estimated respiratory rates and respiratory intervals, respectively for health subjects.
- A reliable heart rate extraction algorithm is proposed by exploiting high-order harmonics and spatial diversity. The MAEs of heart rate estimation of SlpRoF is 0.9 bpm, outperforming a state-of-the-art method by 36%.
- We demonstrate the usefulness of SlpRoF in clinical applications through two case studies. The first study shows that with accurate breathing interval estimation, SlpRoF could detect severe apnea episodes in a patient with 90.6% precision. In the second study of a patient infected with COVID-19, we find that SlpRoF can reliably monitor patient vital signs and characterize recovery trajectories.

The rest of the paper is organized as follows. Section 2 introduces the working principle of IR-UWB radars and experimentally demonstrates the challenges for vital sign monitoring under different body movements and postures

---

[1] The research has received institutional ethics approval for the human subject study.

in sleep. Section 3, 4 and 5 present the entire system design and workflows of SlpRoF. Section 6 reports the evaluation results, and Section 7 presents the results from two clinical case studies. Limitations of the proposed system are discussed in the Section 8. Section 9 gives a brief review of the related works, followed by conclusions in Section 10.

2 BACKGROUND & PRELIMINARY STUDIES

In this section, we first introduce the working principle of IR-UWB radar systems in the context of human sleep monitoring. Then, through case studies we further analyze the challenges of extracting vital sign information in three body movement states and different sleeping postures during sleep.

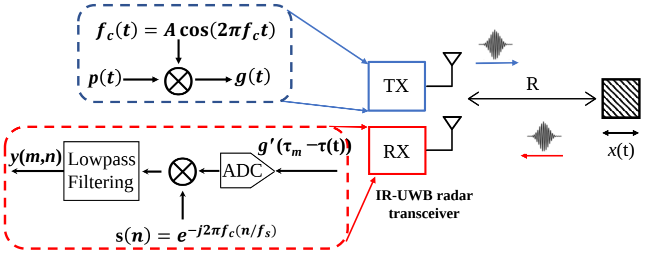

Fig. 1: Single-point scattering model with an IR-UWB radar transceiver.

2.1 Working Principle of IR-UWB Radar

The basic principle of RF-based human sensing is that, under the radiation of RF signals, human physiological motions, such as cardiopulmonary motion and limb movements, change the properties of reflected signals. Therefore, by analyzing the received signals, these motions can be characterized. To explain the principle, we first consider a single-point scattering target in front of an IR-UWB radar transceiver (TRx) as illustrated in Figure 1. R denotes the initial distance between the single-point target and TRx, and $x(t)$ is the displacement of the single-point target over time.

At the radar transmitter (TX), the Gaussian baseband pulse signal $p(t)$ is first modulated by a carrier signal $f_c(t) = cos(2\pi f_c t)$ centered at frequency f_c to generate an RF pulse signal $g(t)$ as:

$$g(t) = p(t - mT_p)\cos(2\pi f_c(t - mT_p)), m = 1, 2, ..., M, \quad (1)$$

where T_p stands for the pulse repetition interval (RPI), index m represents the m-th pulse transmitted by the TX and M is the total number of transmitted pulses. A Gaussian pulse is given by $p(t) = V_G \cdot e^{-t^2/2\sigma^2}$, where V_G is the amplitude of the Gaussian pulse, and σ^2 is the variance corresponding to the -10 dB bandwidth. As the TX emits identical RF pulses periodically, the TX pulse can be rewritten as:

$$g(\tau_m) = p(\tau_m)\cos(2\pi f_c(\tau_m)), \tau_m \in [0, T_p], \quad (2)$$

Due to the variable delay caused by target motion, a received RF pulse signal is expressed as:

$$g'(\tau_m - \tau(t)) = \alpha p(\tau_m - \tau(t))\cos(2\pi f_c(\tau_m - \tau(t))), \quad (3)$$

where α stands for the channel gain, $\tau(t) = 2[R + x(t)]/c$ represents the round-trip time between the radar and the target, and c is the light speed in free space.

In the RX, the received RF pulses are first digitized by a high-speed analog-to-digital converter (ADC) at a sampling rate of f_s. After RF sampling, the received pulse is given by:

$$g_s'(m,n) = \alpha \cdot p(n/f_s - \tau(t_{m,n}))\cos(2\pi f_c(n/f_s - \tau(t_{m,n}))), \quad (4)$$

where $t_{m,n} = mT_p + nT_s, n = 1, 2, ..., N$, N is the total number of samples in each pulse interval, and $T_s = 1/f_s$ stands for the interval between consecutive samples.

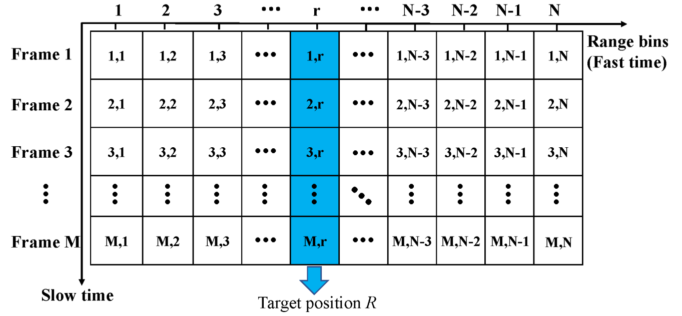

	1	2	3	•••	r	•••	N-3	N-2	N-1	N
Frame 1	1,1	1,2	1,3	•••	1,r	•••	1,N-3	1,N-2	1,N-1	1,N
Frame 2	2,1	2,2	2,3	•••	2,r	•••	2,N-3	2,N-2	2,N-1	2,N
Frame 3	3,1	3,2	3,3	•••	3,r	•••	3,N-3	3,N-2	3,N-1	3,N
⋮	⋮	⋮	⋮	⋮	⋮	⋱	⋮	⋮	⋮	⋮
Frame M	M,1	M,2	M,3	•••	M,r	•••	M,N-3	M,N-2	M,N-1	M,N

Fig. 2: Received baseband matrix.

In the digital domain, the received signal is multiplied by the complex carrier signal $s(n) = V_G \cdot e^{-j2\pi f_c(n/f_s)}$ and then processed by a digital low-pass filter. The resulting complex baseband signal $y(m,n)$ has the following expression:

$$\begin{aligned} y(m,n) &= LPF((g_s'(m,n) \cdot s(n))) \\ &= \frac{\alpha V_G}{2} e^{-\frac{[nT_s - \tau(t_{m,n})]^2}{2\sigma^2}} e^{j2\pi f_c \cdot \tau(t_{m,n})}, \end{aligned} \quad (5)$$

where $LPF(\cdot)$ stands for the process of low-pass filtering. Based on the pulse intervals, the baseband signal $y(m,n)$ can be naturally broken into M frames with the same data length N. As shown in Figure 2, we construct a baseband matrix $y(m,n)$, where each row corresponds to the N samples in the respective frames (pulse interval), known as 'fast time', while elements of the same column are from different frames, called 'slow time'. As fast-time indices are related to the propagation time of RF signals, which is proportional to the range of the target, they are also called *range bins*. For example, with $r = \frac{2R}{c \cdot T_s}$, a target's initial position falls into the r-th range bin.

For human sleep monitoring, Figure 3(a) illustrates the coverage area of a radar placed to the right of and at the same height of the chest of a human subject who lies on a bed. Compared with the aforementioned single-point scatter model, the system model is much more complex in this scenario. A human body spans multiple range bins due to different delays experienced by signals reflected from different on-body positions such as one's left hand, chest, legs, and right hand. As a result, a multi-scatter point model is necessary to describe the received signal as:

$$y^H(m,n) = \sum_{q=1}^{Q} \frac{\alpha_q \cdot V_G}{2} e^{-\frac{[nT_s - \tau_q(t_{m,n})]^2}{2\sigma^2}} e^{j2\pi f_c \cdot \tau_q(t_{m,n})}, \quad (6)$$

where Q is the number of signal channels, including singly reflected paths as well as multiply reflected paths by different parts of the human body and environmental objects. In Equation 6, $\tau_q(t_{m,n}) = 2[R_q + x_q(t_{m,n})]/c$ stands for the

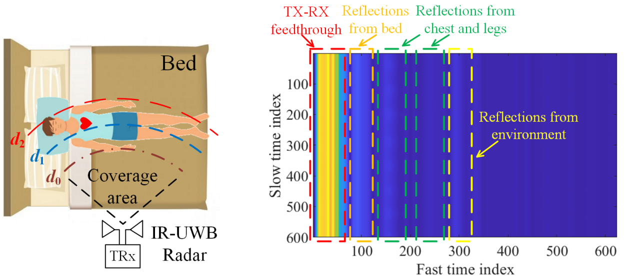

(a) Radar signal coverage. (b) Baseband signal matrix from sleeping human.

Fig. 3: Received baseband matrix from a motionless lying human body.

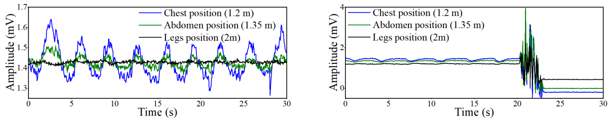

(a) Waveforms extracted from different body positions under motionless state. (b) Waveforms extracted from different body positions under torso movement state.

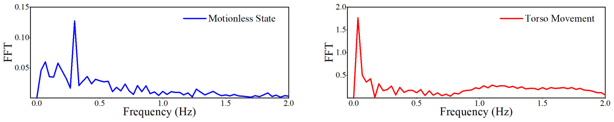

(c) Signal spectrum of respiratory movement. (d) Signal spectrum of torso movement.

Fig. 4: Signal characteristics under different body states.

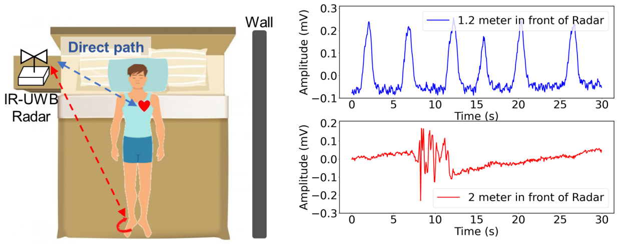

(a) Scenario of leg movement. (b) Waveforms extracted from signals reflected from chest and foot.(Top: chest; Bottom: right foot)

Fig. 5: Effect of leg movement on respiration detection.

signal delay for channel q, where R_q is the distance that the signal travels from the radar to the q^{th} scatter point and $x_q(t_{m,n})$ stands for the displacement due to human physiological activities in the channel. An example of the baseband signal matrix is visualized in Figure 3(b) for sleep monitoring, where 600 frames of data are intercepted with 623 samples in each frame. In Figure 3(b), strong TX-RX feedthrough is concentrated around lower range bins, while the reflected signals from the bed, human chest and legs, and surrounding environments could be found in different range bins. Intuitively, by extracting the slow time signals from these range bins and further analyzing their characteristics, we can categorize body motions over time across these ranges.

2.2 Impacts of Body Motion States on Radar Signals

At the start and during sleep, human bodies undergo different stages of restfulness from twists and turns while trying to fall asleep, to stillness during rapid eye movements (REM), and occasional twitching of legs or even rhythmic movements involving head, limbs, or torso. These movements or the lack of motion manifest differently in captured radar signals. In this section, we conduct a study to investigate the impacts of body states on radar signal characteristics in three scenarios.

In the first scenario, a male subject lies still in bed. Only periodic cardiopulmonary activities are present. 30-s data is captured from an IR-UWB radar for analysis. We extract the signals reflected from the subject's chest position (1.2m), abdomen area (1.35m), and legs (2m), respectively. In Figure 4(a), we can see that the chest-reflected signal (blue curve) fluctuates periodically, and the abdomen-reflected signal (blue curve) also displays periodic fluctuations caused by abdominal respiration. Since the movements in the abdomen area are less than those in the chest area in the supine state, the amplitude of the abdomen-reflected signal is much lower than that of the chest-reflected one. Since subject's legs remain still during data collection, the leg-reflected signal (black curve) is flat.

In the second scenario, the subject is asked to turn over in a 30-s time window to mimic torso movements. Data is also extracted from three areas of interest as shown in Figure 4(b). It is seen that due to the sudden body turnover, all the extracted signals fluctuate significantly, and the rhythm of respiratory activities can no longer be observed. Figure 4(c) and 4(d) show the frequency domain characteristics of chest-reflected signals when the subject is motionless and undergoes torso movements. It is seen that, in the motionless state, a prominent frequency peak could be found at $0.22Hz$, which is close to the subject's actual respiration rate of around 13 bpm. However, during torso movements, due to the abrupt body movement, the spectral peak shifts to $0.02Hz$, which is far lower than the normal respiration rate of healthy people.

In the third scenario, we restrict the subject's motion to limb and hand movements without significant torso movements. Limb movements during sleep can occur periodically or at one time. First, as shown in Figure 5(a), the subject is asked to move his right foot slightly while keeping his chest stationary. The signals reflected from the chest (about 1.2m from the radar) and right foot (about 2m from the radar). Clearly, when his foot moves, the foot-reflected signal exhibits apparent irregularity, whereas the chest-reflected respiration signal remains periodic. This is because the range difference from the radar to the chest and from the radar to the right foot is larger enough such that reflected signals are separable (Figure 5(b)). In the second experiment, as shown in Figure 6(a), the subject is asked to raise his right hand for about 30cm so the singly reflected path between the radar and his chest is occluded, whereas the multiple reflected path from radar to a side wall, his chest and back to the radar is not affected. In Figure 6(b), signal waveforms are extracted from the singly reflected channel at 1.2m and the multi-path channel at

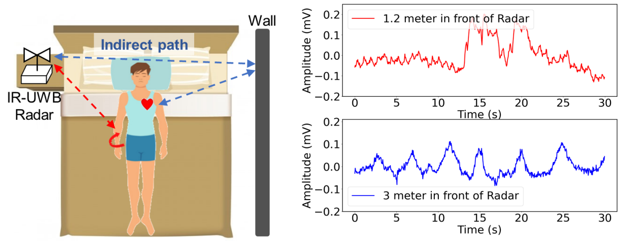

(a) Scenario of hand movement.

(b) Chest-reflected waveform extracted from direct path (1.2m) and indirect path (3m).

Fig. 6: Effect of hand movement on respiration detection.

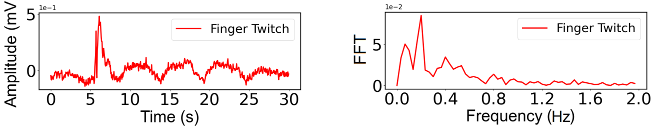

(a) Chest-reflected waveform extracted from direct path.

(b) Signal spectrum corresponding to chest-reflected signal.

Fig. 7: Signal characteristic of finger twitch.

3m for comparison. It can be seen clearly that, though the singly reflected signal (red line) is severely interfered by hand motion, the influence of the hand motion on the multi-path signal is limited, and thus stable respiration (blue line) could still be detected. In the third experiment, the subject places his hand near chest area and twitches his fingers. Figure 7 shows the temporal and spectral signals reflected from his chest. A spike in the signal magnitudes around 6s is clearly visible in Figure 7(a). However, when comparing Figure 4(c) (motionless) and Figure 7(b), we find similar frequency domain characteristics, even though the time domain signals are very different.

In summary, by examining the characteristics of reflected radar signals in different range bins, we have the following observations:

- It is possible to recover vital sign signals during motionless and limb movement states. However, only selected range bins can be utilized.
- With frequency domain features in a selected range bin, it is possible to distinguish motionless from large movement states. However, micro-body movements such as finger twitches may exhibit similar frequency domain characteristics as motionless states.

2.3 Effects of Abnormal Breathing Patterns

Respiratory disorders, such as sleep apnea can introduce abnormal breathing patterns. In this experiment, the subject holds his breath for 25s to mimic sleep apnea. Figure 8 shows the temporal and spectral chest-reflected radar signals captured in a 30-s window. We observe that the peak of the signal spectrum in Figure 8(b) is at a much lower frequency than the normal human respiratory rates, similar to the case with torso movements (Figure 4(d)).

In summary, abnormal breathing has distinct spectral characteristics compared to normal breathing. However, both frequency and time domain features of captured signals are needed to discern the types of body movements, and determine whether one's breathing pattern is normal or not.

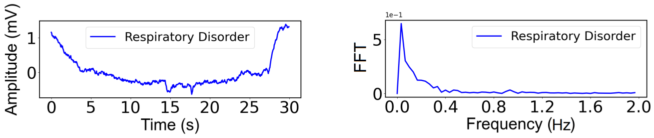

(a) Chest-reflected waveform under sleep apnea.

(b) Signal spectrum corresponding to chest-reflected signal.

Fig. 8: Signal characteristic of sleep apnea.

2.4 Impacts of Body Posture on Heart Rate Extraction

Existing works on radar-based vital sign monitoring typically assume that a radar irradiates directly to the front side of one's chest [26], [27]. Under such an assumption, the strongest heart beat signals coincide in the same range bin as the strongest respiration signals. Consequently, one can first locate a range bin that has the largest respiration fluctuations and then extract heart beat waveforms from the chosen range bin. However, the assumption may not hold for all sleep postures.

In this experiment, as shown in Figure 9(a), the subject sleeps on his right side with the front of his chest obstructed by his arm from the radar. During inhaling and exhaling, his chest and abdomen move at the same rhythm, and thus the reflected signals from both areas contain respiration information. We compute the strength of signals at fixed respiration and heartbeat frequencies in each of the range bins at a distance between 1m (chest) and 1.82m (abdomen). As shown in Figure 9(b), the blue and red lines represent the normalized spectral strength of respiration and heartbeat signals in different range bins. Clearly, the two curves do not always follow the same trend. Specifically, for the respiration signals, peak values are concentrated around 1.3m, which corresponds to the abdomen area. In contrast, for heartbeat signals, peak values lie around 1.12m, which corresponds to the subject's chest area. Clearly, those methods that extract heartbeat signals from the range bin with the highest respiration signal power result in low signal power for heartbeat extraction and possibly wrong heart rate estimation.

Figure 9(c) and Figure 9(d) depict the frequency domain characteristics of the signals reflected from the chest area (at 1.12m) and from his abdomen (at 1.3m). In Figure 9(c), peaks at respiration frequency (around $0.18Hz$) and heartbeat frequency (around $1.15Hz$) as well as their 2^{nd}-order harmonics are evident. In Figure 9(d), a much stronger respiration peak around $0.18Hz$ can be found, and its 3^{rd}-order and 4^{th}-order respiration harmonics are also non-negligible. In contrast, since heartbeat motion is more subtle around the abdominal area, it is challenging to identify the correct heartbeat frequency due to large peaks corresponding to abdominal respiration and its harmonics in this case.

From these experiments, we observe the key barriers to robustly and continuously vital sign monitoring unaddressed by existing methods. We propose SlpRoF, an

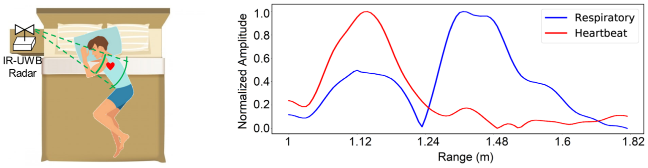

(a) Testing scenario.

(b) Normalized amplitude of respiratory and heartbeat signals over range.

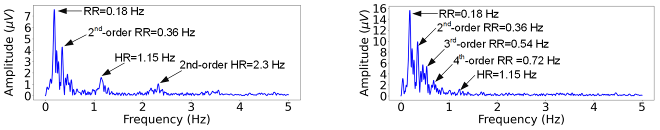

(c) Spectrum of chest-reflected signal.

(d) Spectrum of abdominal-reflected signal.

Fig. 9: Analysis of heart beat extraction in real sleep scenario.

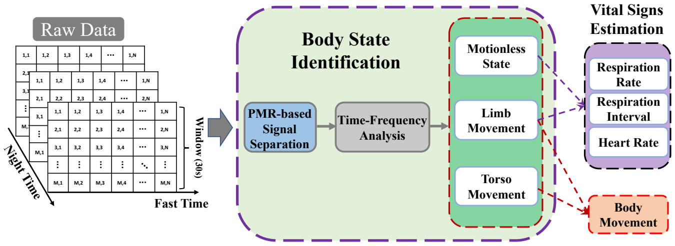

Fig. 10: The system overview of SlpRoF.

RF-based vital sign monitoring solution that answers two questions: 1) how to identify body motion types during which vital signs can be reliably extracted; and 2) how to estimate respiratory profile and heart rates reliably under these motion types and different sleep postures.

3 SYSTEM OVERVIEW

The system diagram of SlpRoF is illustrated in Figure 10. Once the system is turned on, an IR-UWB radar will continuously send and receive RF signals, generating a data stream from the recorded signals. We first use 30-s time windows to divide the overnight data stream and represent the data in each window as a two-dimensional matrix. Next, for each matrix, we identify the state of the human body during these 30-s windows and extract sleep-related physiological parameters. The whole system consists of three modules: raw data segmentation, body state identification, and vital sign estimation. A brief introduction to the latter two modules is presented below:

- **Body State Identification**: This module consists of peak-to-median ratio (PMR) based signal separation, time-frequency analysis, and body state identification. Specifically, we first identify and select the signals that contain human motion information. Then, by exploiting both time and frequency domain signal features, SlpRoF classifies the selected signals into respiration-related signals and body movement-related signals. Next, based on the presence and proportion of both types of signals, it categorizes the subject's motion into *motionless*, *limb movement*, and *torso movement* states.

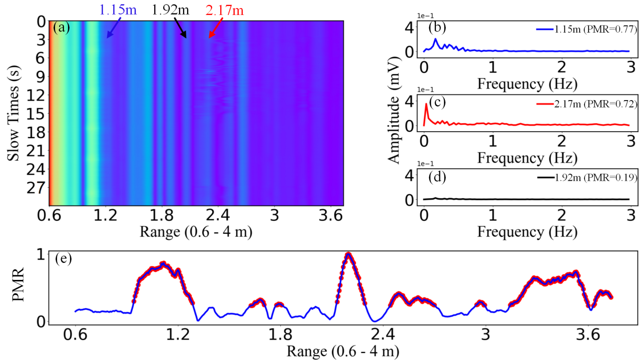

Fig. 11: An example of the reflected signal from different parts of the body within 30s. (a) 2-D baseband matrix of received signal. Spectrum of (b) chest-reflected and (c) leg-reflected signals. (d) Spectrum of stationary signal. (e) PMR distribution across all range bins.

- **Vital Sign Estimation**: When a subject is in motionless and limb movement states, SlpRoF extracts his/her respiratory rates, respiration intervals, and heart rates. Meanwhile, the timing of the torso movements and limb movements are recorded.

In the next sections, we will present in detail how to identify the body motion states and how to extract reliable respiratory profile and heart rates.

4 BODY STATE IDENTIFICATION

In this section, we present the details of the proposed body state identification scheme.

4.1 Removing Reflections from Stationary Ambient Environments

As mentioned previously, when a person lies in front of a radar, signals reflected from different parts of her body fall into different radar range bins, from which, motion information can be extracted for further analysis. However, there are range bins containing signals from ambient environments. Therefore, before extracting vital signs or body movement information, we need to first select range bins that consist of signals from actual body motions.

A key insight is that the signals reflected from stationary ambient environments have steady envelopes. In contrast, macro or micro motions from the human body will introduce variations in magnitude and phase in the time domain, or equivalently peaks in the frequency domain. For the signal $y_i(t)$ in range bin i, we compute its spectrum $Y_i(f)$ via fast Fourier transform (FFT). Define the PMR of the ith range bin as $PMR_i = \frac{\max Y_i(f)}{median(Y_i(f))}$, where $median(\cdot)$ computes the median of a finite series. Range bins with PMR greater than a certain threshold are selected for further analysis. In our implementation, we choose the threshold to be 0.3.

As an example, consider the data collected from a subject who breathes normally with minor foot movements. Figure 11(a) shows the signal energy over time at different distances from a radar. We can observe significant energy

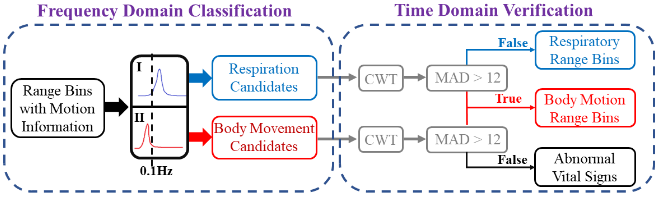

Fig. 12: Range bin classification mechanism.

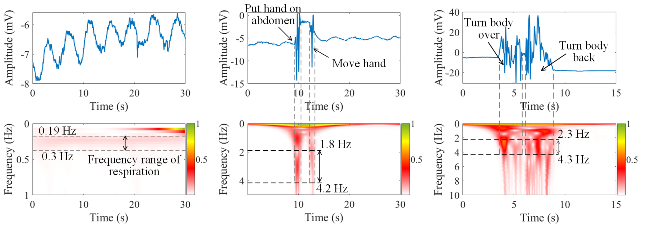

(a) Motionless state. (b) Limb movement state. (c) Torso movement state.

Fig. 13: Signal waveforms and CWT scalograms under different body states.

around 1.2m, which corresponds to the subject's chest. Sudden changes in the signal energy at 9s around 2m, which corresponds to the location of the foot. In contrast, little signal energy or variations can be observed at distance 1.92m. After FFT, noticeable peaks could be found in both Figure 11(b) and Figure 11(c), indicating the presence of body motion, but not in Figure 11(d), due to the lack of any respiration or body movement information. Figure 11(e) shows the PMR values over range bins, where portions exceeding a threshold of 0.3 are highlighted in red.

4.2 Range Bin Classification Based on Time-Frequency Analysis

In the previous step, SlpRoF has selected the range bins containing motion-related information. However, the nature of these motions remains unknown. The motions can be caused by 1) respiration and heat beats, whose resultant signals exhibit periodicity; or 2) limb and torso movements, which tend to be transitory; or 3) abnormal breathing patterns such as long pauses between inhalation and exhalation. As discussed in Section 2.3, frequency domain features alone are insufficient to differentiate the latter two cases. Instead, as illustrated in Figure 12, we propose a two-step procedure by combining frequency and time domain features to classify aforementioned motions from all range bins.

First, we find the main peak position of signals in each range bin in the frequency domain. If the peak frequency of a bin is above $0.1Hz$ (typical respiration frequency is from $0.1Hz$ to $0.6Hz$), the corresponding bin is labeled as a ”respiration candidate”. Otherwise, it is labeled as a ”body movement candidate”. Next, a CWT is applied to the time domain signal in each bin. This is done by convolving the original signal with a pulse signal. If the original signal has a frequency component and time duration similar to the pulse signal, a peak will appear at the corresponding position of the transformed signal after convolution.

The wavelet bases are determined empirically offline. Specifically, we extract the chest waveforms of one human subject under three body states (i.e., motionless state, limb movement, and torso movement) in sleep and compute the CWT scalogram of each waveform by varying the frequency of the wavelet base from $0.07Hz$ to $10Hz$. In Figure 13(a), the time domain signal and the CWT scalogram of a $30s$ episode of motionless state are shown. Stable frequency responses from $0.19Hz$ to $0.3Hz$ can be found in the CWT scalogram, which corresponds to the subject's respiration frequency. For limb movement, sharp disturbance can be observed from the time domain signal in Figure 13(b), as the human subject quickly put his hand on the abdomen at $10s$ and moved the hand away shortly at $12s$. From the CWT scalogram in Figure 13(b), it can be seen that the resultant frequency response of hand movements contains much higher instantaneous frequencies than normal respiration, and wavelets from $1.8Hz - 4.2Hz$ provides a sufficient time resolution to distinguish these two hand movements in time. In the case of torso movements, as shown in Figure 13(c), the human subject turned the body over and back at $3s$ and $6s$, respectively, resulting in rich frequency components over time. Even though the exact time lag between the two movements is hard to identify in the CWT scalogram, the wavelets from $2.3Hz$ to $4.3Hz$ capture the start and end times of the successive torso movements. Based on these observations, SlpRoF chooses a wavelet base with a central frequency of $3.3Hz$ in the implementation.

After CWT, we employ the median absolute deviation (MAD) [28] algorithm to detect outliers in the waveform. If outliers (significant peaks) are bigger than an empirical threshold of 12, we deem that the corresponding bin contains (sudden) body movements. Otherwise, bins that are previously labeled as respiration candidates are classified as containing significant respiration signals. Bins previously labeled as body movement candidates are classified as containing abnormal vital sign signals but no body movements.

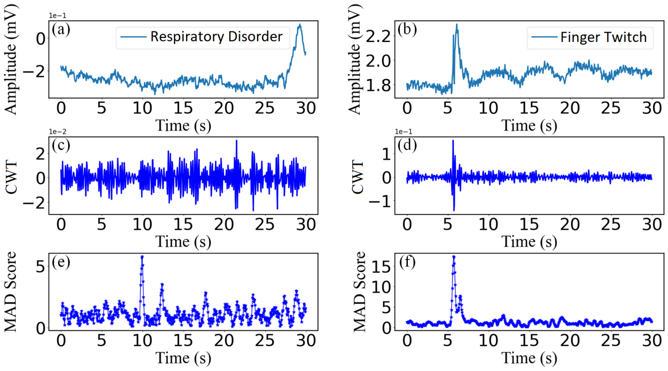

Fig. 14: Signal waveforms before and after CWT and MAD processes. Original signal of (a) respiratory disorder and (b)finger twitch movement. CWT waveforms of (c) respiratory disorder and (d) finger twitch movement. MAD results of (e) respiratory disorder and (f) finger twitch movement.

To illustrate the importance of the second step in distinguishing abnormal respiration patterns and body movements, we show in Figure 14 the time domain signals as well as waveforms after CWT and MAD from finger twitch and abnormal breathing (where the subject is asked to hold breath for about $26s$). The results after CWT for the previous two examples can be observed from Figure 14(c) and 14(d). As shown in Figure 14(c), there is no prominent peak after CWT during abnormal breathing, indicating the absence of abrupt body motion. However, when finger twitching occurs, as shown in Figure 14(d), an obvious peak can be observed at the corresponding position of the resultant CWT waveform. A big difference between their MAD peaks (5 v.s. 15) could be found in Figure 14(e) and 14(f), and with our proposed threshold the abnormal respiration can be differentiated from finger twitch.

4.3 Body State Identification

After the type of each range bin in the radar signal matrix is determined (no motion, body movement, normal respiration, abnormal respiration), we are in the position to identify the state of the body. Recall we are interested in three body states, i.e., *motionless*, *limb movement* only, and *torso movement* states. For a specific time window, if the reflected signal only contains the range bins with signals reflected from normal or abnormal respiratory movements, the human body is in a motionless state. If it contains both the range bins with signal reflected by the respiratory movements and body movements, the human body is in a state of limb movement. Finally, if it contains the range bins with signals reflected by body movement only, we label the subject as in a torso movement state[2].

5 VITAL SIGN ESTIMATION

To this end, we have accurately classified the motion states of a human body during sleep. In this section, we introduce methods for respiration profiling and heart rate estimation.

5.1 Respiration Profiling

When a subject's body is in the motionless state or the limb movement state, we can estimate his/her respiratory profile. Generally, during respiration, human lung exhales and inhales alternatively and rhythmically, so chest reflected signals are steady and periodic. The spectral peak of the signal corresponds to the respiratory rate of the subject. However, respiratory rates can only provide a cursory description of one's respiratory condition. Abnormal breathing patterns due to sleep-related respiratory disorders such as apnea and hypopnea *et al.* [29], [30], [31] can lead to decreased respiratory rates, but such information is insufficient for diagnosis purposes. A comprehensive profiling should include respiratory rate, respiration interval, and the start and end of any prolonged pause in breathing. In SlpRoF, this is accomplished in three steps.

First, we segment signals into 2.5-min long windows with 0.5-min overlapping between neighboring windows. A 4-layer discrete wavelet transform (DWT) is applied to decompose the data of each window into five frequency components ranging from $0-0.625Hz$, $0.625-1.25Hz$, $2.5-5Hz$ and $5-10Hz$. Since typical respiratory rates of human are between $0.1Hz-0.6Hz$, we select the signals in the first band ($0-0.625Hz$) for respiration profiling. Doing so allows us to remove higher-frequency components due to noise or heart beats. Then, in Figure 15, we use two levels of dynamic thresholding to determine respiratory transition points (from inhalation to exhalation). Next, we calculate the time interval between two adjacent transition points as the respiratory interval.

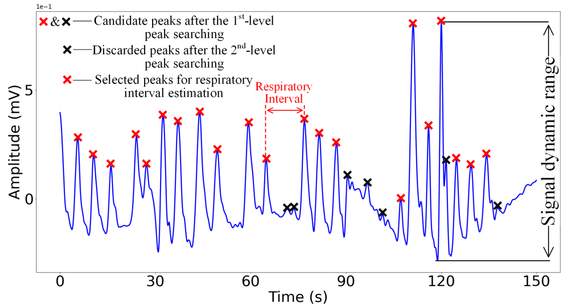

Fig. 15: Identification of transitional points in respiration.

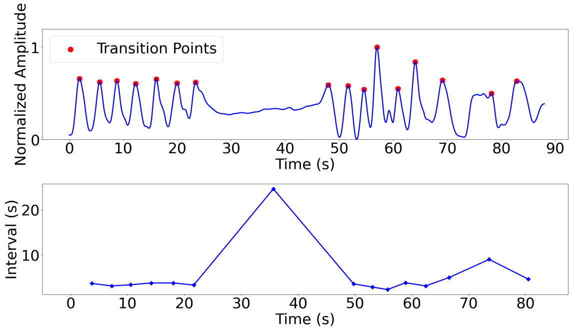

Fig. 16: Respiration interval calculation.

Specifically, at the end of exhalation, one's chest is the furthest from the radar creating a peak in time domain signal. Thus, prominent peaks in the waveform indicate the start and end of respiration cycles. However, due to the presence of noise and other interfering signals, there exist local maximums that are not actual transition points. To eliminate these local maximums, we first compute the dynamic range (γ_w) of the signal in a window w, defined as the difference between the maximum and minimum signal magnitude. Any local maximum with a value less than $\alpha_1 \times \gamma_w$ is discarded. Next, we compute the prominence values of remaining local maximums. Prominence measures how much the peak stands out due to its intrinsic height and its location relative to other peaks [32]. Only those with magnitude higher than α_2 times the median of all prominence values are selected as real transition points. In our implementation, we set $\alpha_1 = 0.01$ and $\alpha_2 = 0.3$.

As an example, in Figure 15, the local maximums with red and black markers exceed the first threshold. After applying the second threshold, only red markers remain. Figure 16 illustrates the computation of respiratory intervals from the detected transition point. In the top plot, there is an obvious pause in respiratory activities from 24s to 48s. Correspondingly, the respiratory interval is estimated to be 24s in the bottom plot.

---

[2] It should be noted that the motion states from the perspective of respiratory sensing are different from actual physical motion states.

Algorithm 1 Heart Rate Extraction

```
Input: Reconstructed signals: $y(i)$, Corresponding Respiratory rate: $f_i^{RR}$. where $i \in N$, and N stands for the set of all selected range bins that contain respiration signal.
for each $i \in N$ do
    $Y_i(f) = FFT(y(i))$
    $Y_i(3f_i^{RR}) = 0$ , $Y_i(4f_i^{RR}) = 0$
    $f_{max} = max(Y_i(f))$, $f_{submax} = max(_{Y_i(f)}Y_i(f_{max}))$
    if $f_{submax} = 2f_{max}$ then
        $HR_{potential}[i] = f_{max} * 60$
    else if $f_{submax} = \frac{2}{3}f_{max}$ then
        $HR_{potential}[i] = \frac{2}{f_{max}} * 60$
    end if
end for
Output: Heart Rate = Median($HR_{potential}$)
```

5.2 Heart Rate Estimation

As discussed in Section 2.4, the range bins with the strongest heartbeat signals and strongest respiration signals do not always coincide. The existence of harmonics of respiration signals in the frequency domain further complicates heartbeat waveform extraction since the latter tends to have a smaller magnitude.

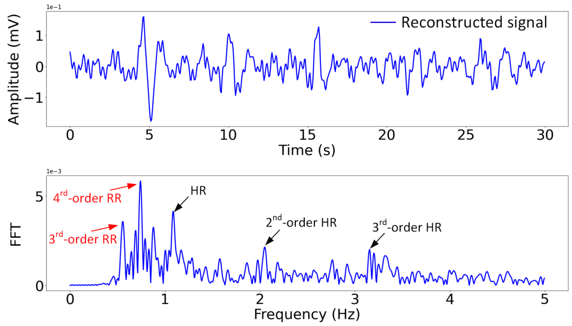

Fig. 17: Reconstruct signals in time (top) and the frequency domain (bottom) for heart rate extraction.

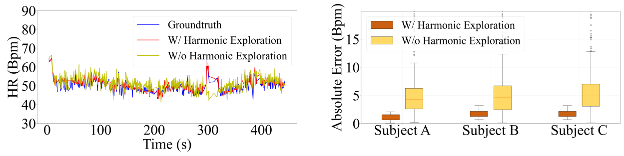

(a) Estimated nocturnal heart rate of subject A.

(b) Heart rate estimation error across different subjects.

Fig. 18: Evaluation of the proposed harmonic exploration technique for heart rate estimation.

Fortunately, as demonstrated in previous research [33], the energy of the higher-order harmonics of respiration signals decays rapidly as the order increases. Therefore, although the low-order harmonics of the respiration signal may be hard to separate from the fundamental frequency of heartbeat signals, the high-order harmonics of the heart rate are less likely to be affected. Consequently, we propose a heart rate extraction method based on the harmonics of heartbeat signals, as shown in Algorithm 1. For each range bin that contains respiration signals, we first use DWT to filter out the respiration and high-frequency interference. Specifically, we sum up the signal components in the frequency range $0.625 - 5Hz$ together to reconstruct a new signal. The newly reconstructed signal only contains the heartbeat signal and strong high-order harmonics of respiration signals as shown in Figure 17.

Next, we take advantage of the aforementioned relationship between heartbeat harmonics and respiratory signal harmonics to estimate heart rate values from the reconstructed signals. Specifically, based on the respiratory rate estimated by the mechanism from Section 5.1, we calculate the spectrum $Y(f)$ of the reconstructed signal and null out the respiration interference in the spectrum by applying notch filters with $0.1Hz$ stop bandwidth whose center frequencies coincident with respiration harmonics. Let the frequencies with the largest and second largest magnitude as f_{max}, and f_{submax}. If $f_{submax} = 2f_{max}$, f_{max} and f_{submax} are the fundamental frequency of the heartbeat and the frequency of its second harmonic, respectively. If $f_{submax} = \frac{3}{2}f_{max}$, f_{max} and f_{submax} are the second and third harmonics of the heartbeat signal, the heart rate is computed as $f_{max}/2$. This procedure is repeated for each range bin that contains respiration signals during motionless or limb movement states. The final heart rate is set to be the median value of the estimated heart rate values in these range bins. Noted that human resting heart rates range from 40 to 100 bpm and respiration rates from 12 to 16 bpm. Therefore, the 3rd or high-order harmonics of respiration can exceed the fundamental frequency of heart wave. As long as the heart rate is not multiple of the respiration rate, the proposed method can suppress the influence of respiration harmonics on heart rate estimation. In the rare situation that the heart rate is exactly multiple of the respiration rate, the notch filter may remove both the 3rd and 4th order respiratory harmonics as well as the fundamental frequency of heartbeats. However, the 2nd and 3rd order harmonics of heart wave will not be suppressed and can still be used for estimation. Therefore, Algorithm 1 can always output a reliable heartbeat frequency despite of the presence of respiratory harmonics.

To evaluate the effectiveness of the proposed harmonic exploration technique for robust heart rate estimation, case studies are conducted on three subjects whose average heart rates are between 48 to 64 bpm. The estimated nocturnal heart rates of subject A with and without the harmonic exploration technique are compared in Figure 18(a), showing that by using the proposed harmonic exploration method a better agreement with the ground truth could be achieved. In Figure 18(b), the distribution of heart rate estimation errors across three subjects demonstrate that the median absolute error could be improved by about 3 bpm with the proposed harmonic exploration technique.

6 EVALUATION

In this section, we evaluate the performance of SlpRoF by conducting experiments in a dormitory and a hotel room with ten volunteers. In both scenarios, SlpRoF outputs the respiratory profile, heart rates, and the timing of body movements during sleep.

TABLE 1: List of sensing devices used in the experiments

Sensor name	Modality	Functions
XETHRU	RF Signal	Body movement Respiratory Profile Heart Rate
VitalPatch	Electrodes	Heart Rate
Camera	Video	Sleep Video Record
Xsens	Inertial Measurement Unit	Body Motion Respiratory Profile

(a) The devices used in our experiment.

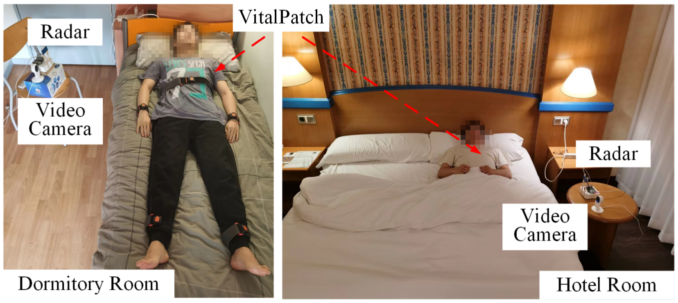

(b) Testing environment.

Fig. 19: Experiment Setup.

6.1 Experiment Setup

The equipment used in the experiments is shown in Figure 19(a) and their corresponding functions are listed in Table 1. The equipment consists of a COTS impulse radio XETHRU module X4M05 [34] and a Raspberry Pi. The radar is connected to the Raspberry Pi via a serial peripheral interface (SPI). The radar transmits $0.4ns$ wide pulses with angle ranges of 65° in azimuth and elevation the center frequency, bandwidth, and sampling frequency of the transmitted signals are $7.3GHz$, $1.4GHz$, and $23.328GHz$, respectively. The frame rate is set to $20Hz$.

We use a camera to record the ground truth bedtime and wake-up times of each subject. VitalPatch [35] is used to obtain the ground truth of heart rates. It is a contact-based heart rate monitoring device, which can accurately measure the heart rates throughout the night with two electrodes attached to the top of a volunteer's heart area. At the same time, five high-precision inertial measurement unit (IMU) devices (Xsens [36]) are used to record body movements. Among the five wearable devices, four are fixed on the limbs, and the remaining one is fixed on a subject's chest. Since Xsens sensors are extremely sensitive to motion, the one fixed on the subject's chest can detect chest movements caused by respiration. Therefore, the respiration rates estimated by conducting FFT on 30-s acceleration data are used as ground truth.

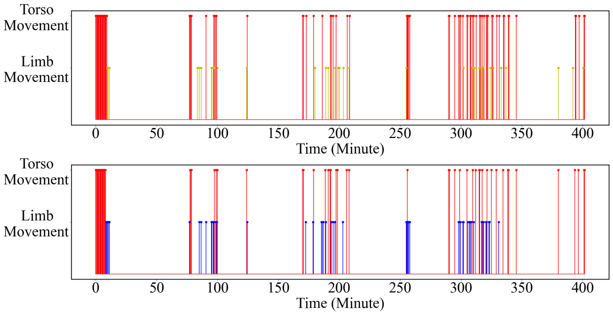

Fig. 20: Comparison of body state estimation results of our proposed radar-based method (top figure) and IMU-based method (bottom figure).

Two indoor environments are chosen with different layouts. As shown in Figure 19(b), the dormitory ($2.7 \times 4m^2$) represents a small space and a multipath-rich environment, while the hotel room ($4.5 \times 5m^2$) represents a regular bedroom.

In both scenarios, the radar is on a bedside table at 0.8-1.2m distance to bed edge to ensure good signal quality. It is placed diagonally above and to the side of the subject's body, with its boresight pointing to the chest area when the human lies face up. Furthermore, the radar antenna needs to be higher than the body when lying on the side to avoid blocking reflected signals in indirect paths. Although we did not test other placements, the poses and the exact position of the subject change over the duration of sleep. Thus, the relative position and orientation of the radar to the subject chest area are not fixed.

6.2 Body State Estimation

We first evaluate the body state estimation performance of SlpRoF. The ground truth results are estimated from the readings of the five IMU sensors placed on the volunteers' bodies. During the experiments, the sampling frequency of the IMU sensors is set to $20Hz$, and a 30-s time window is used to calculate the variance of the acceleration values. A fixed threshold is applied to select the windows with significant movements for IMU sensors. In a time window, if the accelerations of any limb sensors change drastically, limb movements are detected. Similarly, large variations in the chest sensor readings indicate torso movements. Otherwise, the subject is considered to be still.

Figure 20 shows the results of motion states of one subject (volunteer #1) estimated from radar signals and IMU data, respectively, over an overnight period. A lot of torso movements are observed at the beginning of the night because the subject has just gone to bed and has not yet fallen asleep. After a period of stable sleep, the subject experiences unconscious body movements. The estimated results by SlpRoF are mostly consistent with those based on IMU measurements during torso movements and motionless states. However, some limb movements according to the IMU data are estimated as torso movements by SlpRoF.

TABLE 2: Body State Estimation Results

Radar \ IMU	Torso Movement	Limb Movement	Motionless State
Torso Movement	97%	51%	0
Limb Movement	3%	48%	3%
Motionless State	0	1%	97%

Based on our video record, in these cases, the movements of the limbs are too large or occlude the subject's chest area to allow reliable detection of respiratory signals in the radar data.

Table 2 summarizes the confusion matrix of detection results by SlpRoF using those from IMU data as ground truth for all volunteers. SlpRoF can accurately distinguish the torso movements from stillness with 97% estimation accuracy. However, as discussed previously, when some limbs have a large range of motion, SlpRoF confuses the limb movements with torso movements due to the lack of respiratory signals. Such cases account for about half of all limb movements. Importantly, only a small percentage (3%) of actual torso movements, a scenario where respiratory signals may not be reliably extracted, are mistaken as limb movements. From the experiment results, we find that the three different body states (*motionless*, *limb movement*, and *torso movement* states.) account for about 76%, 16%, and 8% of the total sleep time, respectively.

6.3 Respiratory Profiling

After identifying the motion states of the subject, SlpRoF extracts vital sign information when the subject is motionless or with only limb movements. In Figure 21(a), we show the respiratory rates of volunteer #1 over one night. Good agreements can be observed between ground truth value and SlpRoF output. The cumulative distribution functions (CDF) of the absolute errors are given in Figure 21(b). The yellow line represents the overall respiratory rate estimation error of the volunteer #1 based on all three days data. The 80-quantile absolute errors are less than 0.3 bpm, and we break down the CDFs of respiration rate errors according to motion states for both volunteers. It can be observed that the estimation errors are slightly larger when limb movements are present. However, even in this case, 80-quantile and 90-quantile absolute errors are less than 0.3 bpm and 2.2 bpm, respectively. Figure 21(c) compares the CDF of respiration interval estimation of SlpRoF (blue curve) with that of using only the first level of dynamic thresholding for all participants. The respiration intervals are reported only when the subjects are motionless, since ground truth values can only be obtained from IMU sensors when there is no limb or torso movement. We find that 80% of the absolute respiratory interval errors are less than 1.2s. The red line and yellow lines show the respiration interval results according to the methods in [24], [37] with a single one-level threshold $\alpha 1 =$ 0.1 and 0.3, respectively. The result shows that the method with dynamic thresholding significantly outperforms that with a fixed threshold, and its 80-quantile error is lower than the latter by more than 60%.

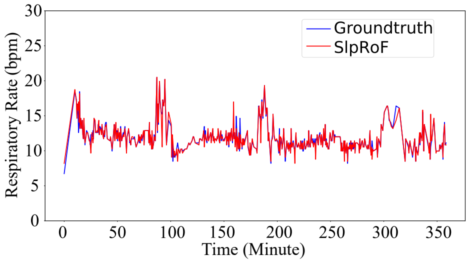

(a) Respiratory rate of volunteer #1.

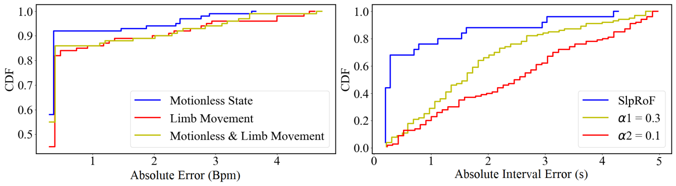

(b) Respiratory rate estimation error distribution. (c) Respiratory interval estimation error distribution.

Fig. 21: Evaluation of respiratory profiling.

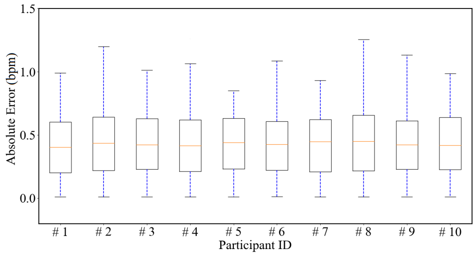

(a) Respiratory rate estimation error for all the volunteers.

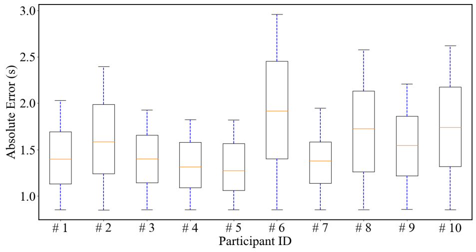

(b) Respiratory interval estimation error for all the volunteers.

Fig. 22: Respiratory rate and respiratory interval estimation errors for all the volunteers.

In Figure 22(a), we show the distribution of respiratory rate estimation errors for all volunteers over three nights. The average MAE is 0.44 bpm, and the average upper quartile absolute error is 0.65 bpm. By setting 5 bpm as the threshold to filter out abnormal respiration rates with an average filter, reliable respiration rates are extracted from 92% of the total sleep time (compared to 76% using the method reported in [38]). We find that 16% of the estimations are from periods under limb movements, which contribute to the improvement of the temporal coverage in SlpRoF. In Figure 22(b), it shows that the average MAE of respiratory interval estimations is around 1.55s, which is adequate for apnea diagnosis.

Figure 23 shows the percentages of reporting time when the absolute respiratory rate errors are below 2 bpm across all participants. Clearly, by including estimations during

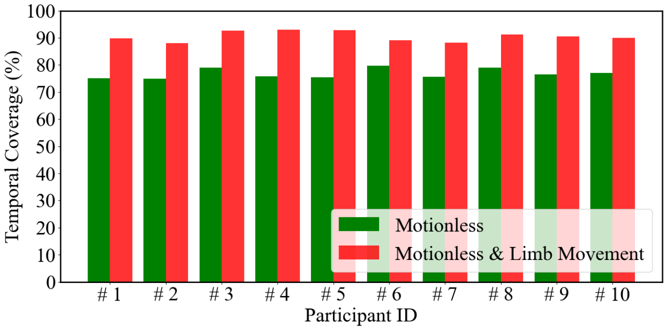

Fig. 23: Respiratory rate estimation coverage for all healthy volunteers.

limb movement states, the temporal coverage improves from 75% to 91%, achieving an improvement of 16%. In other words, SlpRoF under-reports respiratory rates only 9% of the time when they can not in fact be reliably estimated.

6.4 Heart Rate Estimation

In this section, we evaluate the heart rate estimation accuracy of SlpRoF. In Figure 24(a), we show the heart rate estimation results of the volunteer $\#1$ throughout one night. Good agreements can be found between the estimated and the ground truth values.

The CDFs of the absolute errors over 3 nights for volunteer $\#1$ and in different environments are shown in Figure 24(b), we find that in which 80% of the estimation errors for volunteer $\#1$ are less than 1.89 bpm. In the multipath-rich dormitory environment, the 80-quantile estimation error is less than 1.8 bpm, while in the more spacious hotel room, the corresponding error is about 2.4 bpm. SlpRoF achieves more accurate heart rate estimation in the dormitory than in the hotel room because in the dormitory multipath reflections are much richer thus providing more possibilities to excavate heart rates.

Next, we compare the performance of SlpRoF with V^2iFi and Xu et al. The V^2iFi is based on a modified variational modal decomposition (VMD) algorithm. It first decomposes the original radar signals into different components within different frequency bands. Heart rates are then calculated using FFT on the component signals within the heat rate band $1Hz$ to $2Hz$ [25]. For the method in Xu et al. The received signal is first decomposed by the independent component analysis (ICA) algorithm, and then for each signal component, a harmonic-based heart rate selection method is used to calculate heart rate values [39]. The results are shown in Figure 25. Clearly, SlpRoF outperforms both methods in heart rate estimation accuracy. With SlpRoF, The average MAE is 0.9 bpm, and the average upper quartile absolute error is 1.5 bpm. In comparison, with Xu et al. and V^2iFi, the average MAEs are 1.4 bpm and 10.5 bpm, respectively. The V^2iFi method has the poorest performance, because it outputs an estimated heart rate, regardless of the quality of the original signal, resulting in large overall estimation errors. With the proposed harmonic selection-based method, both SlpRoF and Xu et al. are more judicious in choosing suitable range bins for heart rate estimation. As the ICA algorithm in Xu et al. is more sensitive to noise, its estimation accuracy is about 36% lower than SlpRoF. In Figure 26, we plot the percentage of reporting time when the absolute heart rate errors are below 5 bpm across ten participants. We further break down the percentages between motionless and limb movement states. As shown in Figure 26, both SlpRoF and Xu et al. benefit from the inclusion of limb movement periods. Specifically, SlpRoF could reliably estimate heart rates of healthy subjects for 62% of the time in average, achieving about 10% temporal coverage improvement in heart rate estimation. Moreover, due to its high heart rate estimation accuracy, the temporal coverage of SlpRoF is 17% higher than that of Xu et al. This demonstrates the effectiveness of exploiting spatial diversity in our scheme.

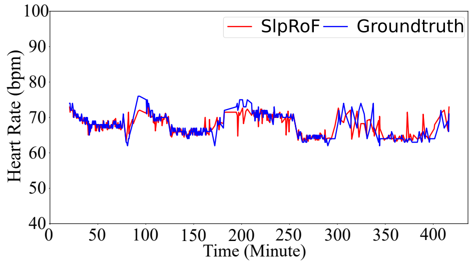

(a) Heart rate of volunteer $\#1$.

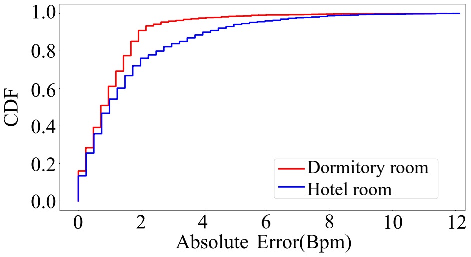

(b) Heart rate estimation error distribution in different scenarios.

Fig. 24: Evaluation of heart rate measurement.

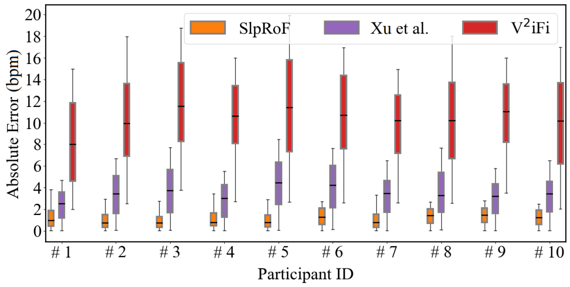

Fig. 25: Heart rate estimation error for all the volunteers.

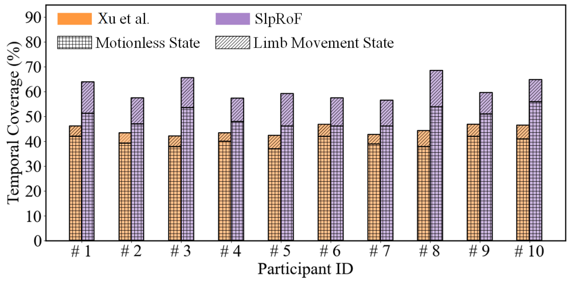

Fig. 26: Heart rate estimation coverage for all the volunteers.

7 CLINICAL CASE STUDY

7.1 Case Study 1: Sleep Apnea Monitoring

The volunteers in the previous experiments were healthy young adults. To understand how well SlpRoF performs when subjects suffer from sleep disorders with abnormal breathing patterns, we conducted an experiment with a patient suffering from severe sleep apnea. Clinically, apnea is diagnosed based on the amount of airflow through the human nasal cavity, blood oxygen level and the movement of the chest and abdomen [40], [41], [42]. When one's nasal cavity airflow is paused for more than 10s and there is no chest or abdomen movement, a patient is diagnosed as in the state of central sleep apnea (CSA). When one's nasal cavity airflow is paused for more than 10s, but the chest and abdomen movements still exist, the patient is diagnosed as suffering from obstructive sleep apnea (OSA). In radar-based contact-free sensing, it is difficult to detect the nasal cavity airflow. Fortunately, when apnea or hypopnea occurs, the amplitude of chest and abdominal movements from respiration decreases significantly. Therefore, with suitable thresholds in peak detection (Section 5.1), it is possible to detect sleep apnea from prolonged respiratory intervals.

In the case study, one patient with severe sleep apnea was recruited. PSG data and radar data are collected simultaneously over night from 21:00 to 5:00 of the next day. During the data collection, the patient is lying on the bed wearing the PSG device, and the radar is located on the right side of the patient, slightly above. We estimate the patient's respiration profile and heart rates during normal periods as well as during episodes of sleep apnea. In particular, in our implementation, when the respiration interval is longer than 10s, an occurrence of sleep apnea is declared by SlpRoF. Six segments of PSG data of two minutes each are used to verify the accuracy of estimated respiratory rates and heart rates, and the whole night's labelled data by a medical doctor is used to calculate the precision of apnea detection.

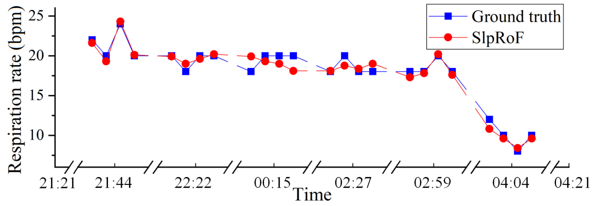

(a) Respiratory rate measurement of SlpRoF and ground truth.

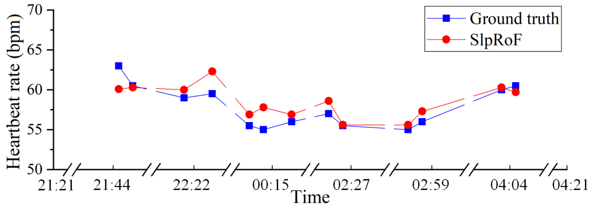

(b) Heart rate measurement of SlpRoF and ground truth.

Fig. 27: Vital sign measurement over night.

The results are shown in the Figure 27. It can be seen that the average and max heart rate estimation errors are 1.28 bpm and 2.9 bpm, respectively, while the average and max respiratory rate estimation errors are 0.6 bpm and 1.8 bpm. Note that there are fewer estimated heart rate values than respiration rates. This is because SlpRoF uses harmonic-based selection and only outputs heart rates when they can be reliably estimated. During the whole night, a total of 58 instances of apnea or hypopnea are detected by a healthcare professional from the PSG data. Among breathing anomalies reported by SlpRoF, 90.6% are indeed true anomalies. However, there are instances of sleep apnea of hypopnea due to the inability of radar sensors to measure airflows.

7.2 Case Study 2: COVID-19 Patient Monitoring

In this section, to explore the utility of SlpRoF for long-term health monitoring, we conduct another experiment with a patient infected by COVID-19. Clinically, COVID-19 patients usually experience a variety of symptoms [43], [44], mostly commonly fever and cough, which lead to increased heart rates and respiratory rates due to shortness of breath. Therefore, by collecting vital signs during sleep, it is possible to characterize the trajectory of their recovery with no human intervention.

In this case study, one patient recently tested positive with COVID-19 was recruited. SlpRoF was utilized to monitor the patient's physiological profile during sleep over seven consecutive nights. Meanwhile, data from VitalPatch and Xsens were used as ground truth for heart rates and respiration rates, respectively. The same setup as shown in Figure 19(b) is used in the experiment. The patient took a daily rapid antigen test (RAT), and was tested positive for all seven days, and then became negative on day 8. With the exception of the first day when the patient had a low level of fever, the patient's body temperature was normal.

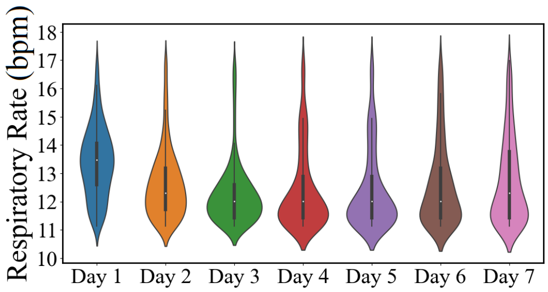

(a) Respiratory rate distribution.

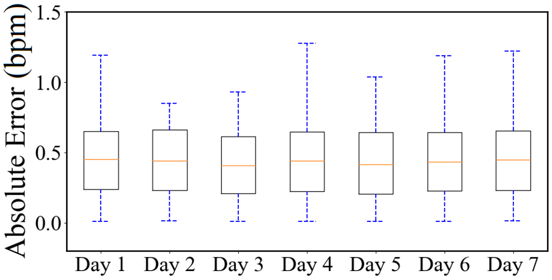

(b) Respiratory rate estimation errors.

Fig. 28: Respiratory rate estimations of a COVID-19 patient over a week.

Figure 28 and Figure 29 illustrate the estimated respiratory rates and heart rates over time and the respective

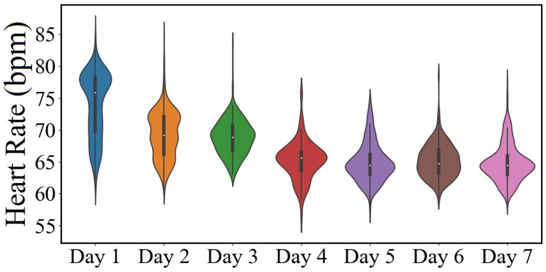

(a) Heart rate distribution.

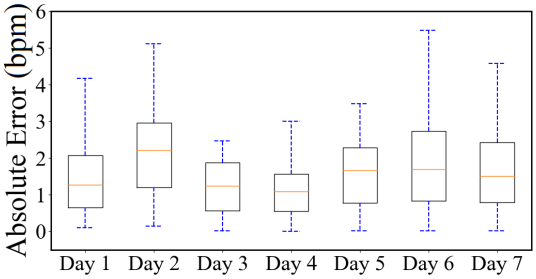

(b) Heart rate estimation errors.

Fig. 29: Heart rate estimation of a COVID-19 patient over a week.

MAEs. From Figure 28(a), it can be observed that, on the first day, the patient's median respiratory rate is around 13.5 bpm and the the respiratory rate throughout the first night varies over a large range. In the subsequent days, the median respiratory rate gradually decreases to 12 bpm, and the distribution of the respiratory rate is more concentrated around the median value. The changes over time are more pronounced in heart rates. As shown in Figure 29(a), the median heart rate is 77 bpm on the first night with large variations through the night. The patient's median heart rate decreased to around 68 bpm on Day 2 and Day 3 and stabilized to around 64 bpm on Day 3 – 7. Variations of heart rates also significantly reduced from Day 2 – 7. The trend in the estimated respiratory rates and heart rates over 7 nights is well aligned with the patient's COVID-19 symptoms. As the patient recovered, the vital signs gradually turned to normal conditions. The absolute errors of estimated respiratory rates and heart rates are shown in Figure 28(b) and 29(b). The MAEs are 0.45 bpm for respiration and 1.8 bpm for heart rates, which are slightly higher than those of healthy subjects.

8 LIMITATIONS AND DISCUSSIONS

In this section, we discuss the limitations of our system and some future research directions.

8.1 Fine-grained Body State Characterization

One's body states during sleep are important sources of sleep physiological information. They are useful in evaluating sleep quality and sleep stages [45], [46], diagnosing sleep disorders such as restless legs syndrome (RLS), insomnia [47], [48], etc.. In SlpRoF, only coarse-grained body states are inferred with the goal of determining when vital signs can be reliably estimated. As discussed in Section 6.2, though the proposed classifier cannot distinguish large limb movements from torso movements if one's chest and abdomen areas are occluded, it significantly improves the temporal coverage of vital sign reporting in SlpRoF. In the future, RF-based fine-grained body state classification can be investigated by looking into diverse techniques, including beamforming-assisted body scanning for skeletal posture estimation [49] and contactless RFID for accurate tracking of specific limb movements [50].

8.2 Monitoring of multiple subjects

In the daily life scenario, it is often important to monitor two or more subjects' vital signs during sleep with RF signals. Benefiting from the cm-level range resolution of the UWB radar in this work, the movements of a single subject's body parts are distinguished and it is also possible to concurrently monitor multiple subjects' sleep. However, owing to the poor angle resolution of this UWB radar, it is difficult to fully isolate subjects' body movements from one another in both direct and indirect paths if they are sufficiently close. In the future, MIMO radars will be considered to increase spatial resolution to realize multi-occupancy sleep monitoring.

8.3 Size of patient population in clinical case studies

Due to the difficulties in recruiting suitable patients who are willing to join the nocturnal test in hospital and at home, only two patients were included in the clinical case study. However, comparable accuracy is achieved for respiratory rate and heart rate estimations for healthy subjects and patients, showing that SlpRoF is promising to be used in clinical settings. In the future, we plan to test the effectiveness of SlpRoF in clinical settings by recruiting more patients.

9 RELATED WORK

Existing work in sleep monitoring can be roughly categorized into two classes: (1) wearable sensor-based methods and (2) RF-based methods.

Wearable Sensor-based Methods: Sensors directly attached to or worn by users can facilitate vital sign monitoring [51]. Dedicated sensors (e.g., ECG sensors and blood pressure sensors) can provide reliable measurements with high accuracy since they are designed and implemented specifically for the purpose of monitoring vital signs. Some wearable devices that have been widely used, such as bracelets, smart watches, etc., can also roughly estimate some physiological parameters, such as sleep quality, heart rates, blood oxygen, etc. Further, Dionisi *et al.* describe an instrumented autonomous T-shirt to monitor respiration rates, heart rates, and body movements [52]. The system containing an electronic circuit board and textile conductive sensors is powered by a solar panel. Meng *et al.* propose a wearable belt integrated with three ECG sensors and an accelerometer to monitor heart condition and assess the level of physical activity [53]. Presti*et al.* attach 12 fiber Bragg grating (FBG) sensors to a textile to monitor the respiratory rates and heart rates in two positions (standing and supine)

TABLE 3: Summary of existing RF-based solutions to vital sign monitoring in the sleep scenario.

Reference	RF device	Deployment	Key methods	Vital sign features	Motion resistance	No. of Subjects/periods	Clinic study
Liu. *et al.* [4]	WiFi	Two sides of the bed	Fine-graind CSI	Resp. and heart rates	No	6 adults/3 months	No
WiFi-Sleep [5]	WiFi	Two sides of the bed	Fine-graind CSI	Resp. rate and depth	No	12 adults/19 nights	No
LungTrack [7]	RFID	Two sides of the bed	RFID based Fresnel zone model	Resp. rate	No	3 adult/2 night	Yes
Turppa. *et al.* [15]	24GHz FMCW	On the ceiling above the bed	Auto-correlation function	Resp. rate and interval; Heart rate and interval	No	11 adults/min-level case study	Yes
Lee. *et al.* [16]	IR-UWB	Above the bed head	Background subtraction and FFT	Resp. rate	No	4 neonates/43 days	Yes
More-fi [22]	IR-UWB	Above the bed head	Deep contrastive learning for fine-grained vital sign waveforms	Resp. rate; Heart rate and interval	Turning-over	12 adults /<80 hours	No
SlpRoF	IR-UWB	One side of the bed	Temporal coverage enhancement	Resp. rate and interval; Heart rate	Portion limb movement	13 adults/ 40 days	Yes

[54]. These wearable vital sign monitoring devices have very high accuracy and can be used as the basis for medical diagnosis. However, they all face some limitations for long-term usage. Portability, comfort, and user acceptance and adherence remain challenges to the wide adoption of such technologies in the home settings.

RF-based Methods: Compared with wearable devices, RF-based methods do not place additional instrumentation on subjects' bodies and are thus inherently device-free [55], [56], [57]. RF sensing is attractive since it can easily provide continuous monitoring using COTS devices at a relatively low cost. For sleep monitoring, in general, researchers first divided human sleep states into body movement state and motionless state and then estimate vital signs under motionless state [17], [18], [20]. In [20], Kwon *et al*. choose the signal with the highest spectral energy to calculate the respiratory rates and heart rates in a motionless state and combine the body movement information and the vital signs to estimate human sleep stages. Moreover, Hsu *et al.* in [58] directly use a neural network to detect whether a person experiences insomnia through the spectrum of the signals bounced off one's body. Studies in [23], [59], [60] use radar systems to detect sleep apnea. By comparing the radar-estimated results with a gold standard, they are trying to find a new standard for the remote detection of apnea. However, existing works usually focus on monitoring specific sleep events such as insomnia, apnea, etc., and lack the detection of fine-grained vital signs. For the few works with vital signs detection capability, it is difficult for them to accurately detect vital signs throughout the night as SlpRoF.

To the best of our knowledge, SlpRoF is the first work that improves the temporal coverage of vital sign estimation in RF-based sleep monitoring. From multipath signal features, we identify motionless, limb movement and torso movement states during sleep and further extract vital sign signals from limb movement states, which significantly increase the total reporting time of vital sign estimations. Furthermore, unlike the existing methods (e.g., MoRe-Fi [21] and MoVi-Fi [22]) that utilize data-driven blackbox models for motion-robust vital sign estimation, SlpRoF takes a principled approach by exploiting harmonic features and multipath spatial diversity. SlpRoF has been validated in long-term sleep studies on healthy subjects as well as through clinical studies. In TABLE 3, we summarize the pros and cons of related works in comparison with our method.

10 CONCLUSION

In this paper, we report our practice of improving the temporal coverage of an RF-based sleep monitoring system, SlpRoF, which provides accurate estimations of respiration rate, respiration interval, and heart rate. By extracting the time-frequency domain features of the reflected signals, SlpRoF classifies body states into three types: *motionless*, *limb movement*, and *torso movement* states and is able to estimate vital signs under some limb movements, which is the key to improve the temporal coverage of physiological profile. Meanwhile, by searching heartbeat harmonics in the spectrum, SlpRoF proposes a reliable heart rate extraction method. We evaluated SlpRoF on ten healthy volunteers and two patients in a variety of settings using commodity hardware. Results demonstrate that SlpRoF outperforms baseline methods in respiration interval and heart rate estimations with higher temporal coverage. Two clinical case studies showed that the outputs from SlpRoF are in line with patients' physical symptoms, and can detect abnormal breathing events. Therefore, SlpRoF goes one step further in monitoring cardiopulmonary health and early in-home diagnosis of sleep disorders.

ACKNOWLEDGMENTS

This work is supported by the European Union through the Horizon EIC pathfinder challenge project SUSTAIN (project number 101071179), the Innovative Medicines Initiative 2 Joint Undertaking under IDEA-FAST project (No. 853981), NSERC Discovery Grant, and the Canada Research Chair program.

REFERENCES

[1] A. Von Ruesten *et al.*, "Association of sleep duration with chronic diseases in the european prospective investigation into cancer and nutrition (epic)-potsdam study," *PloS One*, vol. 7, no. 1, p. e30972, 2012.

[2] V. Tsara *et al.*, "Definition and classification of sleep related breathing disorders in adults: Different types and indications for sleep studies (part 1)," *Hippokratia*, vol. 13, no. 3, p. 187, 2009.

[3] S. Savazzi *et al.*, "Device-free radio vision for assisted living: Leveraging wireless channel quality information for human sensing," *IEEE Signal Processing Magazine*, vol. 33, no. 2, pp. 45–58, 2016.

[4] J. Liu *et al.*, "Tracking vital signs during sleep leveraging off-the-shelf wifi," in *Proceedings of the 16th ACM international symposium on mobile ad hoc networking and computing*, 2015, pp. 267–276.

[5] B. Yu, Y. Wang, K. Niu *et al.*, "Wifi-sleep: Sleep stage monitoring using commodity wi-fi devices," *IEEE Internet of Things Journal*, vol. 8, no. 18, pp. 13 900–13 913, 2021.

[6] F. Zhang *et al.*, "Smars: Sleep monitoring via ambient radio signals," *IEEE Transactions on Mobile Computing*, vol. 20, no. 1, pp. 217–231, 2019.

[7] L. Chen, J. Xiong, X. Chen *et al.*, "Lungtrack: Towards contactless and zero dead-zone respiration monitoring with commodity rfids," *Proceedings of the ACM on Interactive, Mobile, Wearable and Ubiquitous Technologies*, vol. 3, no. 3, pp. 1–22, 2019.

[8] C. Liu, J. Xiong, L. Cai, L. Feng, X. Chen, and D. Fang, "Beyond respiration: Contactless sleep sound-activity recognition using rf signals," *Proceedings of the ACM on Interactive, Mobile, Wearable and Ubiquitous Technologies*, vol. 3, no. 3, pp. 1–22, 2019.

[9] J. Liu, X. Chen, S. Chen, X. Liu, Y. Wang, and L. Chen, "Tagsheet: Sleeping posture recognition with an unobtrusive passive tag matrix," in *IEEE INFOCOM 2019-IEEE Conference on Computer Communications*. IEEE, 2019, pp. 874–882.

[10] Y. Lee *et al.*, "A novel non-contact heart rate monitor using impulse-radio ultra-wideband (ir-uwb) radar technology," *Scientific Reports*, vol. 8, no. 1, pp. 1–10, 2018.

[11] K.-K. Shyu *et al.*, "Detection of breathing and heart rates in uwb radar sensor data using fvpief-based two-layer eemd," *IEEE Sensors Journal*, vol. 19, no. 2, pp. 774–784, 2018.

[12] Y. Rong and D. W. Bliss, "Direct rf signal processing for heart-rate monitoring using uwb impulse radar," in *2018 52nd Asilomar Conference on Signals, Systems, and Computers*. IEEE, 2018, pp. 1215–1219.

[13] N. Regev and D. Wulich, "Remote sensing of vital signs using an ultra-wide-band radar," *International Journal of Remote Sensing*, vol. 40, no. 17, pp. 6596–6606, 2019.

[14] Y. Wang *et al.*, "Vital sign monitoring in dynamic environment via mmwave radar and camera fusion," *IEEE Transactions on Mobile Computing*, 2023.

[15] E. turppa *et al.*, "Vital sign monitoring using fmcw radar in various sleeping scenarios," *Sensors*, vol. 20, no. 22, p. 6505, 2020.

[16] W. H. Lee *et al.*, "Non-contact sleep/wake monitoring using impulse-radio ultrawideband radar in neonates," *Frontiers in Pediatrics*, vol. 9, p. 782623, 2021.

[17] S. Yue, Y. Yang, H. Wang, H. Rahul, and D. Katabi, "Bodycompass: Monitoring sleep posture with wireless signals," *Proceedings of the ACM on Interactive, Mobile, Wearable and Ubiquitous Technologies*, vol. 4, no. 2, pp. 1–25, 2020.

[18] S. Yue, H. He, H. Wang, H. Rahul, and D. Katabi, "Extracting multi-person respiration from entangled rf signals," *Proceedings of the ACM on Interactive, Mobile, Wearable and Ubiquitous Technologies*, vol. 2, no. 2, pp. 1–22, 2018.

[19] J. Lai, Z. Yang, and B. Guo, "A two-stage low-complexity human sleep motion classification method using ir-uwb," *IEEE Sensors Journal*, vol. 21, no. 18, pp. 20 740–20 749, 2021.

[20] H. B. Kwon *et al.*, "Attention-based lstm for non-contact sleep stage classification using ir-uwb radar," *IEEE Journal of Biomedical and Health Informatics*, vol. 25, no. 10, pp. 3844–3853, 2021.

[21] T. Zheng, Z. Chen, S. Zhang, C. Cai, and J. Luo, "More-fi: Motion-robust and fine-grained respiration monitoring via deep-learning uwb radar," in *Proceedings of the 19th ACM Conference on Embedded Networked Sensor Systems*, 2021, pp. 111–124.

[22] Z. Chen, T. Zheng, C. Cai, and J. Luo, "Movi-fi: Motion-robust vital signs waveform recovery via deep interpreted rf sensing," in *Proceedings of the 27th Annual International Conference on Mobile Computing and Networking*, 2021, pp. 392–405.

[23] Y. Zhou *et al.*, "Validation of novel automatic ultra-wideband radar for sleep apnea detection," *Journal of thoracic disease*, vol. 12, no. 4, p. 1286, 2020.

[24] N. Du, K. Liu, L. Ge, and J. Zhang, "Apnearadar: A 24ghz radar-based contactless sleep apnea detection system," in *2017 2nd International Conference on Frontiers of Sensors Technologies (ICFST)*. IEEE, 2017, pp. 372–376.

[25] T. Zheng, Z. Chen, C. Cai, J. Luo, and X. Zhang, "V2ifi: In-vehicle vital sign monitoring via compact rf sensing," *Proceedings of the ACM on Interactive, Mobile, Wearable and Ubiquitous Technologies*, vol. 4, no. 2, pp. 1–27, 2020.

[26] M. Yang, X. Yang, L. Li, and L. Zhang, "In-car multiple targets vital sign monitoring using location-based vmd algorithm," in *2018 10th International Conference on Wireless Communications and Signal Processing (WCSP)*. IEEE, 2018, pp. 1–6.

[27] C. Li and J. Lin, "Random body movement cancellation in doppler radar vital sign detection," *IEEE Transactions on Microwave Theory and Techniques*, vol. 56, no. 12, pp. 3143–3152, 2008.

[28] T. Pham-Gia and T. L. Hung, "The mean and median absolute deviations," *Mathematical and Computer Modelling*, vol. 34, no. 7-8, pp. 921–936, 2001.

[29] D. W. Hudgel, "Sleep apnea severity classification—revisited," *Sleep*, vol. 39, no. 5, pp. 1165–1166, 2016.

[30] A. M. Sanchez *et al.*, "Central sleep apnea and atrial fibrillation: A review on pathophysiological mechanisms and therapeutic implications," *IJC Heart & Vasculature*, vol. 30, p. 100527, 2020.

[31] M. P. Mansukhani, B. P. Kolla, Z. Wang, and T. I. Morgenthaler, "Effect of varying definitions of hypopnea on the diagnosis and clinical outcomes of sleep-disordered breathing: a systematic review and meta-analysis," *Journal of Clinical Sleep Medicine*, vol. 15, no. 5, pp. 687–696, 2019.

[32] "8 peak detection," in *Data Analysis and Signal Processing in Chromatography*, ser. Data Handling in Science and Technology, A. Felinger, Ed. Elsevier, 1998, vol. 21, pp. 183–190.

[33] Y. Rong and D. W. Bliss, "Remote sensing for vital information based on spectral-domain harmonic signatures," *IEEE Transactions on Aerospace and Electronic Systems*, vol. 55, no. 6, pp. 3454–3465, 2019.

[34] XeThru Radar Sensor, (Accessed: May 19, 2022). [Online]. Available: https://novelda.com/

[35] C. M. Areia *et al.*, "A chest patch for continuous vital sign monitoring: Clinical validation study during movement and controlled hypoxia," *Journal of Medical Internet Research*, vol. 23, no. 9, p. e27547, 2021.

[36] XSens IMU Sensor, (Accessed: May 19, 2022). [Online]. Available: https://www.xsens.com/

[37] M. Baboli, A. Singh, B. Soll *et al.*, "Wireless sleep apnea detection using continuous wave quadrature doppler radar," *IEEE Sensors Journal*, vol. 20, no. 1, pp. 538–545, 2019.

[38] T. Rahman, A. T. Adams, R. V. Ravichandran *et al.*, "Dopplesleep: A contactless unobtrusive sleep sensing system using short-range doppler radar," in *Proceedings of the 2015 ACM International Joint Conference on Pervasive and Ubiquitous Computing*, 2015, pp. 39–50.

[39] H. Xu *et al.*, "Accurate heart rate and respiration rate detection based on a higher-order harmonics peak selection method using radar non-contact sensors," *Sensors*, vol. 22, no. 1, p. 83, 2021.

[40] C. Hirotsu, J. Haba-Rubio, D. Andries *et al.*, "Effect of three hypopnea scoring criteria on osa prevalence and associated comorbidities in the general population," *Journal of Clinical Sleep Medicine*, vol. 15, no. 2, pp. 183–194, 2019.

[41] M. S. Badr and S. Javaheri, "Central sleep apnea: a brief review," *Current pulmonology reports*, vol. 8, no. 1, pp. 14–21, 2019.

[42] C. Kalkbrenner, M. Eichenlaub, S. Rüdiger, C. Kropf-Sanchen, R. Brucher, and W. Rottbauer, "Validation of a new system using tracheal body sound and movement data for automated apnea-hypopnea index estimation," *Journal of Clinical Sleep Medicine*, vol. 13, no. 10, pp. 1123–1130, 2017.

[43] J. Matta, E. Wiernik, and O. Robineau, "Association of self-reported covid-19 infection and sars-cov-2 serology test results with persistent physical symptoms among french adults during the covid-19 pandemic," *JAMA INTERNAL MEDICINE*, vol. 182, no. 5, pp. 579–579, 2022.

[44] A. Maloberti *et al.*, "Heart rate in patients with sars-cov-2 infection: Prevalence of high values at discharge and relationship with disease severity," *Journal of Clinical Medicine*, vol. 10, no. 23, p. 5590, 2021.

[45] N. Naito, M. Kikuchi, Y. Yoshimura *et al.*, "Atypical body movements during night in young children with autism spectrum disorder: A pilot study," *Scientific reports*, vol. 9, no. 1, pp. 1–10, 2019.

[46] N. Furutani, T. Takahashi, N. Naito, T. Maruishi, Y. Yoshimura, C. Hasegawa, T. Hirosawa, and M. Kikuchi, "Complexity of body movements during sleep in children with autism spectrum disorder," *Entropy*, vol. 23, no. 4, p. 418, 2021.

[47] C. Piano, A. Losurdo, G. Della Marca *et al.*, "Polysomnographic findings and clinical correlates in huntington disease: a cross-sectional cohort study," *Sleep*, vol. 38, no. 9, pp. 1489–1495, 2015.

[48] G. Didato, R. Di Giacomo, G. J. Rosa *et al.*, "Restless legs syndrome across the lifespan: symptoms, pathophysiology, management and daily life impact of the different patterns of disease presentation," *International Journal of Environmental Research and Public Health*, vol. 17, no. 10, p. 3658, 2020.

[49] A. Sengupta, F. Jin, R. Zhang, and S. Cao, "mm-pose: Real-time human skeletal posture estimation using mmwave radars and cnns," *IEEE Sensors Journal*, vol. 20, no. 17, pp. 10 032–10 044, 2020.

[50] X. Liu, D. Liu, J. Zhang, T. Gu, and K. Li, "Rfid and camera fusion for recognition of human-object interactions," in *Proceedings of the 27th Annual International Conference on Mobile Computing and Networking*, 2021, pp. 296–308.

[51] A. J. Bandodkar, I. Jeerapan, and J. Wang, "Wearable chemical sensors: Present challenges and future prospects," *Acs Sensors*, vol. 1, no. 5, pp. 464–482, 2016.

[52] A. Dionisi, D. Marioli, E. Sardini, and M. Serpelloni, "Autonomous wearable system for vital signs measurement with energy-harvesting module," *IEEE Transactions on Instrumentation and Measurement*, vol. 65, no. 6, pp. 1423–1434, 2016.

[53] Y. Meng, S.-H. Yi, and H.-C. Kim, "Health and wellness monitoring using intelligent sensing technique," *Journal of Information Processing Systems*, vol. 15, no. 3, pp. 478–491, 2019.

[54] D. L. Presti, C. Massaroni, D. Formica *et al.*, "Smart textile based on 12 fiber bragg gratings array for vital signs monitoring," *IEEE Sensors Journal*, vol. 17, no. 18, pp. 6037–6043, 2017.

[55] H. Wang, D. Zhang, J. Ma, Y. Wang, Y. Wang, D. Wu, T. Gu, and B. Xie, "Human respiration detection with commodity wifi devices: Do user location and body orientation matter?" in *Proceedings of the 2016 ACM international joint conference on pervasive and ubiquitous computing*, 2016, pp. 25–36.

[56] Y. Zeng, D. Wu, J. Xiong, E. Yi, R. Gao, and D. Zhang, "Farsense: Pushing the range limit of wifi-based respiration sensing with csi ratio of two antennas," *Proceedings of the ACM on Interactive, Mobile, Wearable and Ubiquitous Technologies*, vol. 3, no. 3, pp. 1–26, 2019.

[57] Y. Zeng, D. Wu, J. Xiong, J. Liu, Z. Liu, and D. Zhang, "Multisense: Enabling multi-person respiration sensing with commodity wifi," *Proceedings of the ACM on Interactive, Mobile, Wearable and Ubiquitous Technologies*, vol. 4, no. 3, pp. 1–29, 2020.

[58] C.-Y. Hsu, A. Ahuja, S. Yue, R. Hristov, Z. Kabelac, and D. Katabi, "Zero-effort in-home sleep and insomnia monitoring using radio signals," vol. 1, no. 3, 2017.

[59] S. Kang, D.-K. Kim, Y. Lee, Y.-H. Lim, H.-K. Park, S. H. Cho, and S. H. Cho, "Non-contact diagnosis of obstructive sleep apnea using impulse-radio ultra-wideband radar," *Scientific reports*, vol. 10, no. 1, pp. 1–7, 2020.

[60] N. Thi Phuoc Van *et al.*, "Microwave radar sensing systems for search and rescue purposes," *Sensors*, vol. 19, no. 13, p. 2879, 2019.

Pei Wang (Student Member, IEEE) received the MS degree in computer sciense and technology from Northwestern Polytechnical University, Xi'an, China, in 2020. He is currently working toward the Ph.D degree at the Ambient Intelligence and Pervasive System Group, Institut Polytechnique de Paris, France. His current research interests include biomedical application of microwave, millimeter-wave and ubiquitous wireless sensing.

Xujun Ma (Member, IEEE) received the Ph.D. degree in information and communication engineering from Southeast University, Nanjing, China, in 2020. Since 2020, he has been a Postdoctoral Research Fellow with the Ambient Intelligence and Pervasive System Group, Télécom SudParis, Évry, France. His current research interests include biomedical application of microwave, millimeter-wave CMOS circuit design, and wireless sensing. He was the Second-Place Award recipient of the Student Paper Competition of 2019 IEEE-IMBioC.

Rong Zheng (Senior Member, IEEE) received her Ph.D. degree from Dept. of Computer Science, University of Illinois at Urbana-Champaign and earned her M.E. and B.E. in Electrical Engineering from Tsinghua University, P.R. China.She is now a Professor in the Dept. of Computing and Software in McMaster University, Canada. She was on the faculty of the Department of Computer Science, University of Houston from 2004 to 2012. Rong Zheng's research interests include mobile computing, data analytics and networked systems. She is currently Tier-1 Canada research chair in Mobile Computing. She was awarded the NSERC Discovery Accelerator Supplement in 2019 and received the National Science Foundation CAREER Award in 2006, and was a Joseph Ip Distinguished Engineering Fellow from 2015 - 2018.

Luan Chen (Member, IEEE) received the Ph.D. degree from Conservatoire National des Arts et Métiers (CNAM-Paris) in 2020. He is currently an associate professor with the Information, Communications and Imaging (ICI) group of ETIS laboratory (UMR 8051), a joint research laboratory of CY Cergy Paris University, ENSEA and CNRS in France. His research interests span the fields of wireless indoor localization/sensing, statistical signal processing (RF/biomedical), mobile computing for IoT and machine learning technologies.

Xiaolin Zhang received the Ph.D. degree in Peking University Health Science Center, BeiJing, China, in 2013. She is currently an associate chief physician in the Department of Geriatrics, Peking University First Hospital, Beijing, China. She is an expert in lung disease, aging care and geriatric medicine.

Djamal Zeghlache (Life Member, IEEE) received the Ph.D. degree in electrical engineering from Southern Methodist University, Dallas, TX, USA, in 1987. He was an Assistant Professor with Cleveland State University from 1987 to 1991. In 1992, he joined Télécom SudParis, Institut Mines-Telecom, where he acts as a Professor and the Head of the Wireless Networks and Multimedia Services Department. His current research concerns architectures, protocols, and interfaces for future networks addressing cloud, SDN, and NFV optimization, control, and management reinforced by data-driven approaches and in network intelligence.

Daqing Zhang (Fellow, IEEE) received the Ph.D. degree from the University of Rome "La Sapienza," Italy, in 1996. He is currently a Chair Professor with the Key Laboratory of High Confidence Software Technologies, Ministry of Education, School of Computer Science, Peking University, China; and Telecom SudParis, IP Paris, France. He has authored more than 300 technical papers in leading conferences and journals. His research interests include context-aware computing, urban computing, mobile computing, big data analytics, and pervasive elderly care. He is the Winner of the Ten-Years CoMoRea Impact Paper Award at IEEE PerCom 2013 and the Ten-Years Most Influential Paper Award at IEEE UIC 2019, the Honorable Mention Award at ACM UbiComp 2015 and 2016, and the Distinguished Paper Award at ACM UbiComp 2021. He was the general chair or the program chair for more than 17 international conferences, giving keynote talks at more than 20 international conferences. He is an Associate Editor for the IEEE PERVAS IVE COMPUTING, *ACM Transactions on Intelligent Systems and Technology*, and the Proceedings of the *ACM on Interactive, Mobile, Wearable and Ubiquitous Technologies*.